

Article

Analysis of Effects of Surface Roughness on Sensing Performance of Surface Plasmon Resonance Detection for Refractive Index Sensing Application

Treesukon Treebupachatsakul ¹, Siratchakrit Shinnakerdchoke ¹ and Suejit Pechprasarn ^{2,*} 

¹ Department of Biomedical Engineering, School of Engineering, King Mongkut's Institute of Technology Ladkrabang, Bangkok 10520, Thailand; treesukon.tr@kmitl.ac.th (T.T.); 61011333@kmitl.ac.th (S.S.)

² College of Biomedical Engineering, Rangsit University, Pathum Thani 12000, Thailand

* Correspondence: suejit.p@rsu.ac.th

Abstract: This paper provides a theoretical framework to analyze and quantify roughness effects on sensing performance parameters of surface plasmon resonance measurements. Rigorous coupled-wave analysis and the Monte Carlo method were applied to compute plasmonic reflectance spectra for different surface roughness profiles. The rough surfaces were generated using the low pass frequency filtering method. Different coating and surface treatments and their reported root-mean-square roughness in the literature were extracted and investigated in this study to calculate the refractive index sensing performance parameters, including sensitivity, full width at half maximum, plasmonic dip intensity, plasmonic dip position, and figure of merit. Here, we propose a figure-of-merit equation considering optical intensity contrast and signal-to-noise ratio. The proposed figure-of-merit equation could predict a similar refractive index sensing performance compared to experimental results reported in the literature. The surface roughness height strongly affected all the performance parameters, resulting in a degraded figure of merit for surface plasmon resonance measurement.

Keywords: surface plasmon resonance; sensing performance; refractive index sensing; surface roughness; instrumentation



Citation: Treebupachatsakul, T.; Shinnakerdchoke, S.; Pechprasarn, S. Analysis of Effects of Surface Roughness on Sensing Performance of Surface Plasmon Resonance Detection for Refractive Index Sensing Application. *Sensors* **2021**, *21*, 6164. <https://doi.org/10.3390/s21186164>

Academic Editors: Andrea Cataldo, Emanuele Piuzzi and Agnieszka Szyplowska

Received: 23 August 2021
Accepted: 11 September 2021
Published: 14 September 2021

Publisher's Note: MDPI stays neutral with regard to jurisdictional claims in published maps and institutional affiliations.



Copyright: © 2021 by the authors. Licensee MDPI, Basel, Switzerland. This article is an open access article distributed under the terms and conditions of the Creative Commons Attribution (CC BY) license (<https://creativecommons.org/licenses/by/4.0/>).

1. Introduction

Surface plasmons are oscillations due to moving electrons that exist at an interface between conductors and dielectrics [1]. This phenomenon can generate a resonating effect when illuminated by an external electric field called surface plasmon resonance (SPR) [2]. The theory of SPR has been utilized for numerous sensing technology and applications, including host–pathogen detection [3,4], protein interactions [5,6], ultrasonic detections [7], refractive index sensing [8,9], voltage sensing [10], and microscopic imaging application [11,12]. For example, Lan et al. [13] reported the binding kinetics of SARS-CoV-2 and angiotensin-converting enzyme 2 (ACE2) using SPR measurement.

The surface plasmon polariton (SPP)-based sensor can be classified into two primary configurations: Otto [14] and Kretschmann [15] configurations, as shown in Figure 1a,b [6]. A beam of p-polarized coherent incident light penetrates through a glass prism, illuminates the thin noble metal surface, and reflects off the metal surface.

Figure 2 depicts reflectance dips, called surface plasmon resonance dips, and the minimum position of the dip is called plasmonic angle θ_{sp} due to the coupling process [16] and the quantum light–matter interaction between photons and electrons [17]. The θ_{sp} position is sensitive to changes in external conditions around the metal surface, such as the refractive index of surrounding media, noble metal thickness, and incident light wavelength. These enable numerous label-free sensing technologies [18,19]. The blue and red curves in Figure 2 were calculated using rigorous coupled-wave theory [20,21] for a

water-based environment with a refractive index of the sensing region n_s of 1.33, bovine serum albumin (BSA) at a concentration of 80 mg/mL with a refractive index n_s of 1.35 [22].

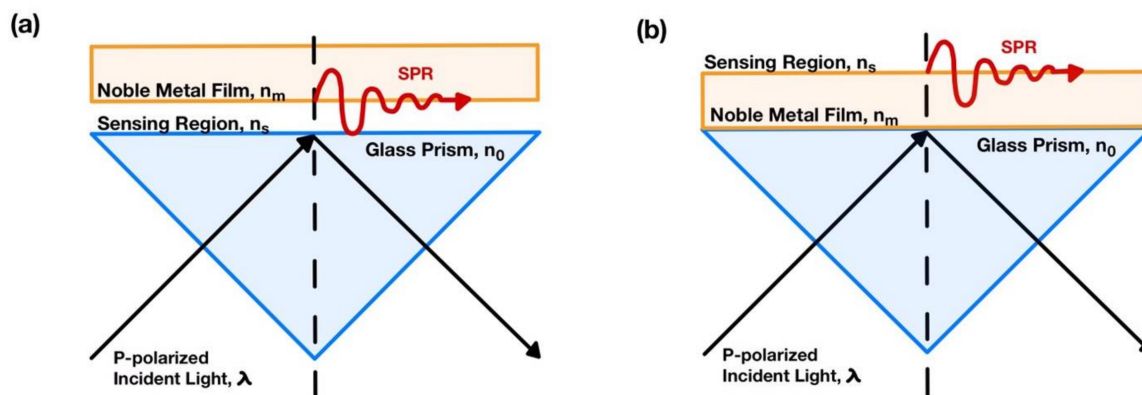


Figure 1. (a) The Otto configuration; and (b) the Kretschmann configuration.

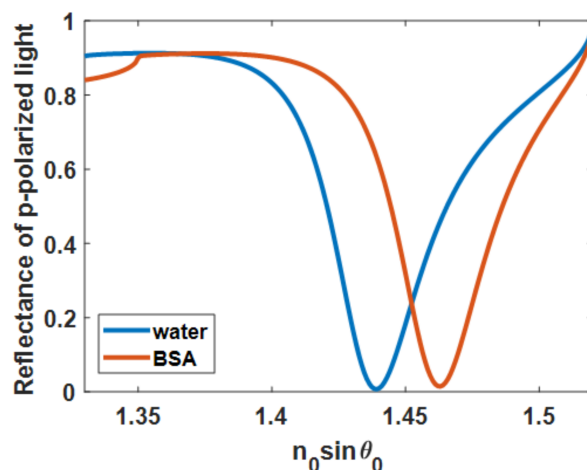


Figure 2. Reflectance spectra of uniform 50 nm gold on BK7 glass substrate when the gold sensor was illuminated by p-polarized coherent light at 633 nm. The blue curve showed the reflectance spectrum when the sample sensing region was water, and the red curve showed the reflectance spectrum when the sample sensing region was BSA protein solution with a sample refractive index of 1.35.

The difference between the Kretschmann configuration and the Otto configuration is that the Otto configuration requires a narrow spacing gap; the gap is typically a wavelength or subwavelength thickness. Although Shen et al. [8] and Pechprasarn et al. [23] reported that the Otto configuration could provide higher sensitivity, the gap has burdened fabrication demand. As a result, SPR sensors usually employ the Kretschmann configuration and have become more commonly known as the traditional SPR-based sensor [24]. The effect of surface roughness for the Kretschmann configuration and Otto configuration is similar; hence, the Otto result was omitted to shorten the length of the manuscript.

Smooth plasmonic sensors can be achieved through chemical polishing [25,26], using mica substrate [27], the stripping method [28,29], self-limiting galvanic displacement [30], chemically grown single-crystalline gold [31], laser ablation [32], helium ion beam [33], and thermal annealing [34]. Table 1 shows the remaining roughness of the plasmonic gold sensor after different surface treatments.

Table 1. Shows surface roughness and surface smoothing methods.

Method	Remaining Root Mean Square (RMS) Roughness
No treatment: sputter coating	RMS = 1.2 nm
Chemical polishing [25,26]	RMS = 0.38 ± 0.05 nm
Mica substrate utilizing [27]	RMS = 0.2 nm
Chemically grown single-crystalline gold [31]	RMS < 1 nm
Laser ablation [32]	RMS = 0.17 nm
Helium ion beam [33]	RMS = 0.267 nm
Thermal annealing [34]	RMS < 1 nm

For sensitivity-demanding applications, such as single-molecule detection [35] and small-molecule measurements [36], it is established that the smoothness and uniformity of plasmonic metal play a crucial role in sensing performance [37–40] and electrical conductivity [41]. In addition, the roughness can introduce additional ohmic loss to the surface wave attenuation coefficient [11].

Theoretical papers on SPR sensors [35,42,43] have reported the theoretical sensitivity for SPR calculated using ideally smooth metal surfaces. In addition, the effects of roughness on SPR characteristics, resonant conditions [44] and reflectance [45], transmittance, and absorption spectra [46] have been reported and investigated. For example, research groups have proposed a dispersion-relation model [45,47] and measured a rough-surface plasmon sensor's propagation length [48]. In addition, Yang et al. [49] experimentally validated that the plasmonic angle depended on the roughness of the metal film using the surface-annealing method.

For sensing applications, the effect of roughness on the sensitivity is established [50,51]: the roughness can degrade the bulk sensitivity; however, it also can enhance the binding sensitivity due to the enhanced localized surface plasmon and an increased surface area for the chemical reaction [52]. Byun et al. [52] proposed a theoretical model quantifying the sensitivity for different roughness using a binary grating model. However, the sensitivity alone cannot provide a complete justification of the sensing performance since the sensitivity does not consider the quality factor (Q factor) describing how narrow the plasmonic dip is [53].

The current trend and the state-of-the-art technology for SPR measurement are to measure smaller biological molecule size [54,55] and numbers of molecules [56,57], aiming towards single-molecule detection [58]. In addition, SPR measurement methods have been proposed to enhance the sensitivity in SPR measurement, including phase detection [59,60], long-range surface plasmon polaritons [61], and metamaterial surfaces [62,63]. There are, of course, challenges in achieving such measurements, including environmental stability and the quality of the plasmonic sensor surface. This study has excluded all the other factors and quantified the effects of the sensor's surface roughness, providing an indicator for estimating the expected SPR sensing performance.

This research aims to provide a theoretical framework to analyze and quantify the effects of surface roughness of the surface plasmon resonance sensor on sensing performance parameters, including sensitivity, optical intensity at the plasmonic angle, position of plasmonic dips, full width at half maximum (FWHM), and figure of merit (FOM) using rigorous coupled-wave analysis and Monte Carlo simulations. Thus, the relevant sensing parameters provide an insight into the effects of roughness on the bulk refractive index measurement performance. In addition, we believe the paper provides a complete assessment of how the roughness affects the bulk refractive index sensing measurement and how far from the theoretical limit can be expected for a plasmonic sensor with a roughness range.

2. Materials and Methods

2.1. Surface Plasmon Resonance Detection and Rough Surface Model

The simulation structure, as illustrated in Figure 3, consisted of (1) a p-polarized helium–neon laser (HeNe) source at 633 nm wavelength λ , (2) a glass substrate made of BK7 glass with a refractive index of 1.52, and (3) uniform and rough gold layers with a refractive index of $0.18344 + 3.4332i$ [64] and average thicknesses of $50 \text{ nm} - h$ and h , respectively. The h term is the arithmetic mean thickness of the rough surfaces. A unit cell length of $1 \mu\text{m}$ was chosen and represented 1000 pixels based on the sampling theory to ensure that the unit cell accommodated different roughnesses, ranging from the minimum of 1 nm to the maximum of 50 nm. For the 50 nm case, the unit cell of $1 \mu\text{m}$ had 20 different roughness peaks, mimicking a genuine surface-roughness nature.

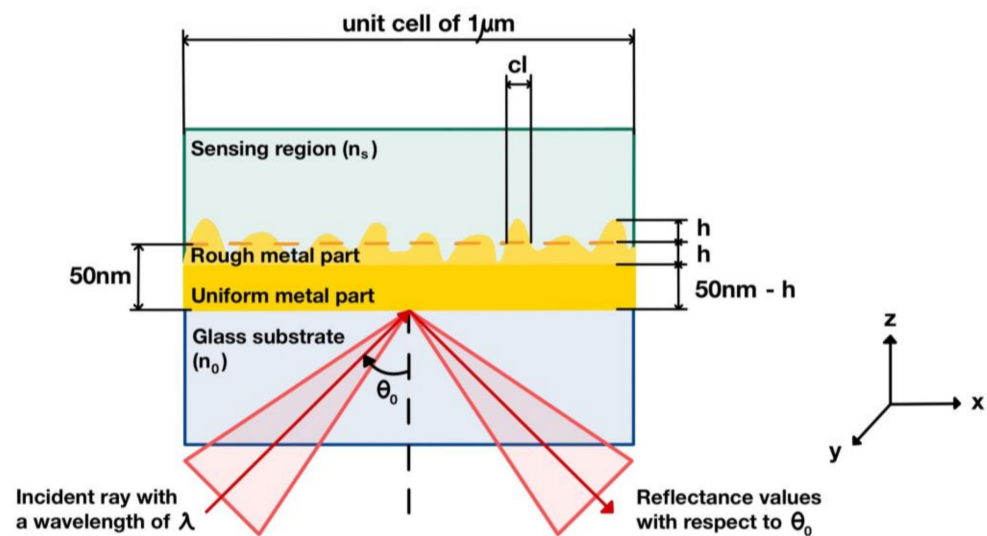


Figure 3. Simulation diagram including roughness parameters required for constructing rough surface profiles.

The overall metal layer thickness was also fixed at 50 nm. The 50 nm gold layer was an optimum gold thickness for a sensing application since it gives the lowest intensity plasmonic dip [65]. The roughness was defined using two parameters: the average height of the rough surface h and the correlation length cl . This study's range of h and cl was 1 nm to 20 nm and 1 nm to 50 nm, respectively. The range of h and cl were chosen so that the roughness profiles covered the conventional SPR excitation and the SPR mode cut-off positions for the two variables, as shown later in the Results section. The following steps adopted from Byun et al. [52] are for simulating the rough surface profiles:

- (1) Generate a random surface profile $h(x)$ with digital numbers 0 and 1 and multiply by the expected h , where x is the spatial distance along the x -axis of the substrate, as depicted in Figure 4a.
- (2) Fourier transform the generated surface $H(f_x) = \mathcal{F}[h(x)]$, where $H(f_x)$ is the Fourier-transformed profile, f_x is the Fourier domain axis, and \mathcal{F} is the Fourier-transform operator, as depicted in Figure 4b.
- (3) Low-pass filter the Fourier surface profile using the Gaussian distribution function $G(f_x)$ expressed as shown in Equation (1) and depicted by red curves in Figure 4b.

$$G(f_x) = \exp\left(-x^2 / \left(cl^2 / 2\right)\right) \quad (1)$$

- (4) Inverse Fourier transform the product of $\mathcal{F}^{-1}\{H(f_x) \cdot G(f_x)\}$ to obtain the rough surface profile, as depicted in Figure 4c.

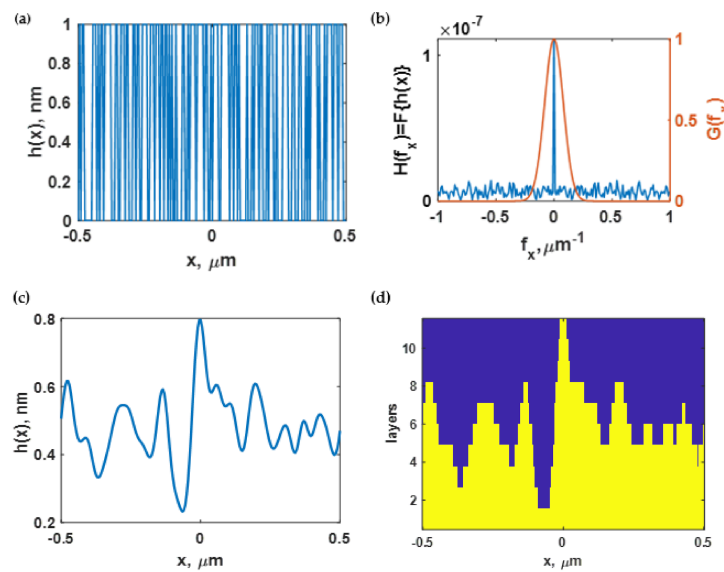


Figure 4. (a) Product of h and a sequence of randomized 0 and 1; (b) magnitude of $H(f_x)$ after Fourier transform (indicated as the blue curve) and a Gaussian distribution plot determined by cl (shown as the red curve); (c) inverse Fourier transform of the product $H(f_x) \cdot G(f_x)$, resulting in a rough surface structure; and (d) the 10-layer rough gold surface and a single-layer uniform gold surface.

The other approach to define the roughness is the root mean square (RMS) of the surface profile given by Equation (2):

$$RMS = \sqrt{\int_{-0.5\mu m}^{0.5\mu m} [h(x) - \bar{h}]^2 dx} \quad (2)$$

The rough surface profile was then converted into the rough gold surface, represented by 10 layers for rigorous coupled-wave analysis calculation. The surface profile was modeled in a rectangular coordinate system. In addition, the area below the surface profile was the gold material with the refractive index of $0.18344 + 3.4332i$ [64], while the upper area was the sensing region with a refractive index of n_s shown in Figure 4d. Finally, the constructed rough surface was assembled with a uniform gold layer thickness of $50 \text{ nm} - h$ before proceeding with the optical-simulation process.

2.2. Optical Simulation Using Rigorous Coupled-Wave Analysis

Rigorous coupled-wave analysis (RCWA) [21,66] was employed to compute the reflectance spectrum of the SPR detection platforms for different rough surfaces. The RCWA software was developed in-house in the MATLAB environment utilizing the parallel computing and graphic processing toolboxes. All the simulations reported in the manuscript were simulated using 151 diffraction orders to ensure that all the cases achieved convergence. The numerical stability and accuracy for the 151 diffracted orders were within 0.0028, corresponding to a numerical error of 0.28%. The convergent tests for all the extreme cases in the manuscript are reported and discussed later in Section 3.1.

Since the rough surfaces were generated randomly, Monte Carlo simulation, which is very effective for estimating the results from an uncertain event [67], was applied in this study. The computation proceeded with the RCWA simulation 100 times per one set of roughness parameters as depicted by the process flow in Figure 5 to ensure that the recovered quantitative parameters described in the next section were stable for any single pair of height h and correlation length cl .

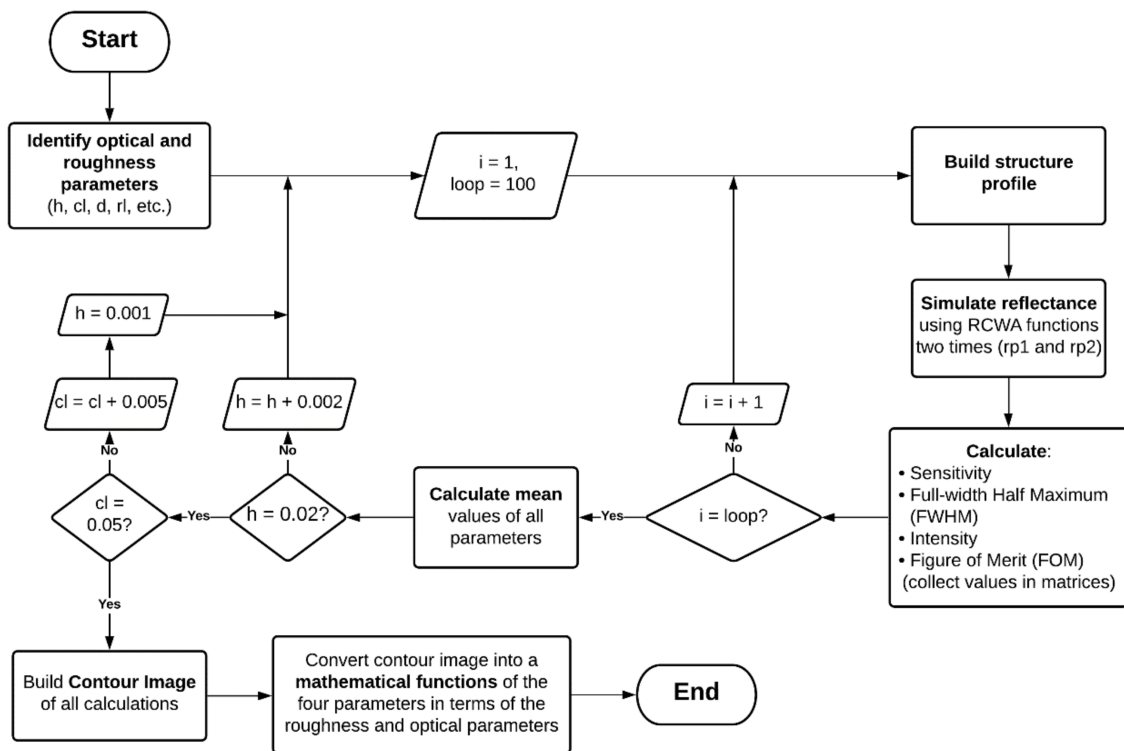


Figure 5. Flowchart of the simulation and calculation processes, including structure profile construction, RCWA, and sensor-quality computation.

2.3. Quantitative Performance Parameters

The RCWA simulation was applied to compute optical reflectance responses for the sensing region n_s with a refractive index of 1.33 (water) and 1.35 (bovine serum albumin protein solution) [68] to quantify the bulk sensitivity response of the rough surfaces. The quantitative performance parameters were: sensitivity (S), full width at half maximum ($FWHM$), intensity difference (ΔI), dip intensity at the plasmonic angle (I_{sp}), and figure of merit (FOM).

- (1) Sensitivity (S) was defined as the change in plasmonic wave vector (k_{sp}) over the change in refractive index (n_s) in the sensing region, as depicted in Figure 6a and expressed in Equation (3). The unit of S is $\text{rad} \cdot \text{RIU}^{-1} / \mu\text{m}$. Note that RIU stands for refractive index unit.

$$S = \frac{\Delta k_{sp}}{\Delta n_s} = \frac{2\pi n_0 \Delta \sin \theta_{sp}}{\lambda \Delta n_s} \quad (3)$$

- (2) The full width at half maximum ($FWHM$) was defined as the average width of the SPR dips with the n_s of 1.33 and 1.35 cases in wave-vector space with an optical intensity of at least 0.5 (50%) of the normalized optical reflectance spectra, as depicted in Figure 6b and expressed in Equation (4). Thus, the unit of the $FWHM$ is $\text{rad} / \mu\text{m}$.

$$FWHM = \frac{\Delta k_{nor,1.33} + \Delta k_{nor,1.35}}{2} \quad (4)$$

where $\Delta k_{nor,1.33}$ and $\Delta k_{nor,1.35}$ are the $FWHM$ of the normalized SPR reflectance spectra when the refractive index of the sensing region was 1.33 and 1.35, respectively.

- (3) Intensity contrast (ΔI) was the average change in optical reflectance at the two plasmonic dips, as shown in Figure 6a and expressed by Equation (5):

$$\Delta I = \frac{|\Delta I_{1.33}| + |\Delta I_{1.35}|}{2} \quad (5)$$

where $\Delta I_{1.33}$ and $\Delta I_{1.35}$ are the change in optical reflectance at the plasmonic angles when the refractive index of the sensing region was 1.33 and 1.35, respectively.

- (4) Optical reflectance at the plasmonic angle (I_{sp}) was defined as the average optical reflectance ($I_{sp1.33}$ and $I_{sp1.35}$) of the two plasmonic dips when the refractive index of the sensing region was 1.33 and 1.35, as expressed in Equation (6):

$$I_{sp} = \frac{I_{sp1.33} + I_{sp1.35}}{2} \quad (6)$$

- (5) The figure of merit (FOM) was defined by considering the dip movement, the $FWHM$, and the intensity level. Here, the FOM was defined as shown in Equation (7):

$$FOM = \frac{\Delta I \times S}{I_{sp} \times FWHM} = \frac{\Delta I \times \Delta k_{sp}}{I_{sp} \Delta n_s FWHM} \quad (7)$$

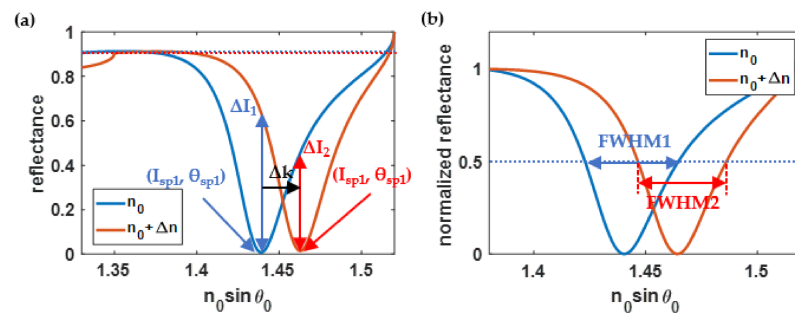


Figure 6. (a) Calculation methods of all quantitative performance parameters of the surface plasmon resonance detection; and (b) normalized optical reflectance and the full width at half maximum (FWHM).

3. Results and Discussion

3.1. Convergence Test of Extreme Cases

The roughness range studied was the cl of 1 nm to 50 nm and the h of 1 nm to 20 nm. Therefore, the four boundary cases were: (1) cl of 1 nm and h of 1 nm; (2) cl of 1 nm and h of 20 nm; (3) cl of 50 nm and h of 1 nm; and (4) cl of 50 nm and h of 20 nm. Figure 7 shows the convergence test by varying the number of diffracted orders included in the RCWA calculations using the p-polarized wave at a 633 nm wavelength, and the incident angle was at the plasmonic incident angle $n_0 \sin \theta_{sp}$ of 1.50 for case (1), 1.43 for case (2), 1.44 for case (3), and 1.48 for case (4); the convergence of all the cases was reached. The numerical fluctuations between 149 diffracted orders and 151 diffracted orders were 0.28%, 0.24%, 0.17%, and 0.04%, respectively.

The convergent tests for the four extreme cases in the study showed that the diffracted order of 151 orders achieved the numerical stability of 0.28%, and the convergence was reached. Of course, the number of diffracted orders could be increased to achieve higher numerical precision; this, of course, would come with increased demand for computing time and resources. Therefore, the subsequential results were computed using 151 diffracted orders.

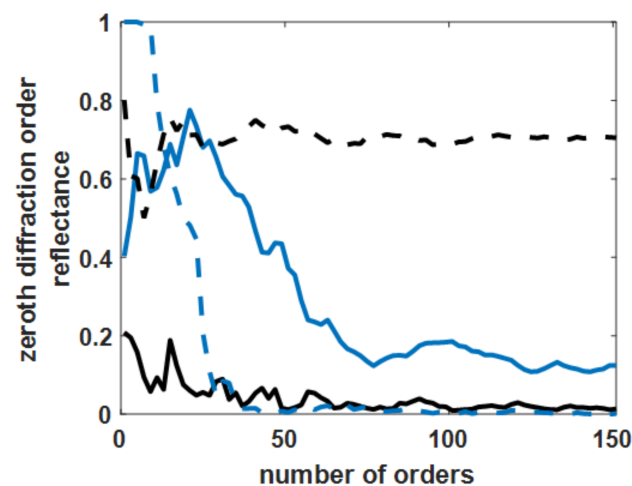


Figure 7. Optical reflectance of the p-polarization for four levels of rough surfaces with the varying number of diffracted orders included in the RCWA calculations. Note that the solid blue curve is for cl of 1 nm and h of 1 nm, the dashed blue curve is for cl of 1 nm and h of 20 nm, the solid black curve is for cl of 50 nm and h of 1 nm, and the dashed blue curve is for cl of 50 nm and h of 20 nm.

3.2. Effect of Roughness on the SPR Sensitivity

Figure 8a shows the sensitivity calculated using Equation (3) and the RCWA simulation with the Monte Carlo model described in Sections 2.2 and 2.3 for different roughness profiles generated as described in Section 2.1. The sensitivity depended strongly on the roughness of the gold sensor. For the smooth surface, the sensitivity was $7.47 \text{ rad} \cdot \text{RIU}^{-1} / \mu\text{m}$. The sensitivity degraded when the cl decreased and h increased. Note that the larger cl indicated a smoother surface. The SPR responses shown in Figure 8a were categorized into three regions labeled as ‘SPR’, ‘Negative movement SPR’, and ‘No SPR’. The SPR label was for the roughnesses for which the SPR dip responded to the change in the higher sample refractive index by the dip movement towards the larger plasmonic angle, as shown in Figure 8b. In addition, at a specific level of roughness with an h value ranging between 4 and 8 nm, the sensitivity slightly increased to just above $7.50 \text{ rad} \cdot \text{RIU}^{-1} / \mu\text{m}$. On the other hand, there was a region where the plasmonic angle moved slightly towards a lower coupling incident angle, such as at h of 9 nm and cl of 15 nm, as shown in Figure 8c. The third region was labeled ‘No SPR’; no plasmonic dip appeared in the reflectance spectra, as shown in Figure 8d.

The sensitivity contour shown in Figure 8a could then be selected based on the area of interest, with h and cl ranging from 0 nm to 9 nm and 35 nm to 50 nm, respectively. It was then normalized to the maximum sensitivity and the curve fitted to the fifth-degree polynomial function $S(h, cl)$ using a built-in curve-fitting toolbox in MATLAB. The curve-fitted model expressed in Equation (8) had a coefficient of determination R^2 of 99.80%. Figure 9a shows the curve-fitted contour calculated using Equation (8). Note that the normalized sensitivity was curve-fitted using different polynomial degrees ranging from the 2nd-order to the 5th-order polynomial function, and calculated the R^2 for each polynomial curve-fitting function. The reason for limiting to the 5th order polynomial was that higher orders could distort the shape of the fitted curve by fitting with high-frequency components, including noise artifacts in the model. The general practice for curve fitting is to start with low polynomial order and calculate the corresponding R^2 and absolute or root-mean-square error between the fitted contour and the curve-fitting function. The error should appear as random noise with no noticeable shapes and patterns, as shown in Figure 9b. Then, the optimal polynomial order can be tested by curve-fitting the contour with a higher-order polynomial and determining error. The higher-order polynomial can be employed before the error contour begins to form a noticeable pattern; in other words, a distortion between the contour and the curve-fitting model. Here, the fifth-degree polynomial function was

chosen since it provided the highest R^2 value. The curve-fitted equation was then validated by calculating the absolute error, comparing the normalized sensitivity contour calculated using RCWA to the parameter calculated using the curve-fitted equations as shown in Figure 9b. The maximum error shown in Figure 9b was 0.015, which was well below 1.5%. The curve-fitting procedure was also adopted to model the other performance parameters in the subsequent sections.

$$\begin{aligned}
 S(h, cl) = & -1.31 + 4348h + 161.3cl - (8.11 \times 10^5)h^2 - (3.02 \times 10^5)hcl \\
 & - 3751cl^2 + (8.38 \times 10^6)h^3 + (5.54 \times 10^7)h^2cl \\
 & + (6.88 \times 10^6)hcl^2 + (2.88 \times 10^4)cl^3 + (5.10 \times 10^7)h^4 \\
 & - (5.24 \times 10^8)h^3cl - (1.23 \times 10^9)h^2cl^2 \\
 & - (5.15 \times 10^7)hcl^3 + (2.04 \times 10^{10})h^5 \\
 & - (1.47 \times 10^{10})h^4cl + (9.77 \times 10^9)h^3cl^2 \\
 & + (8.64 \times 10^9)h^2cl^3
 \end{aligned} \quad (8)$$

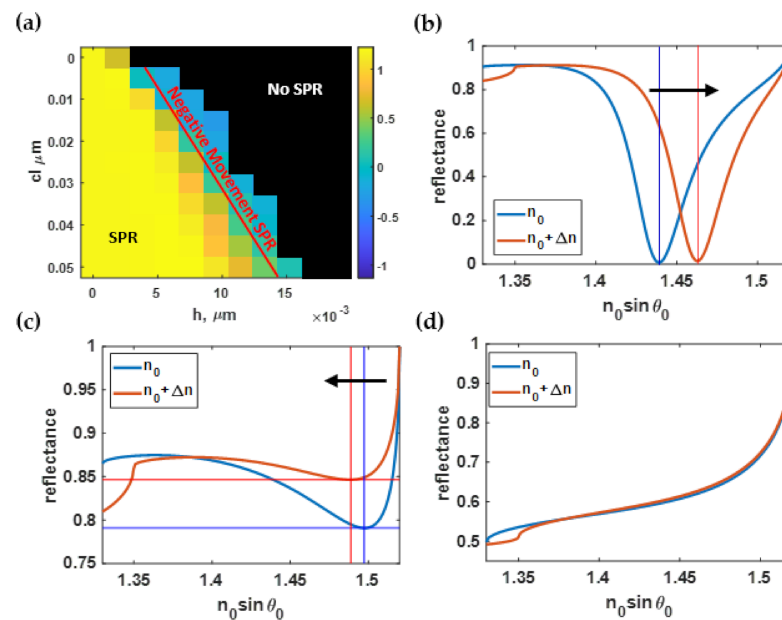


Figure 8. (a) Sensitivity calculated using Monte Carlo simulation; (b) SPR dips at h of 1 nm and cl of 50 nm; (c) negative SPR dip movement at h of 9 nm and cl of 15 nm; and (d) reflectance when there was no SPR dip present at h of 15 nm and cl of 5 nm.

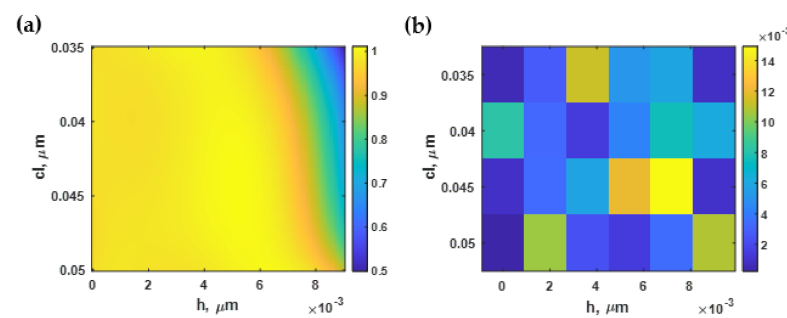


Figure 9. (a) The normalized sensitivity based on Equation (8); and (b) the difference between Equation (8) and the RCWA simulation.

The normalized sensitivity contour in Figure 9a shows that the roughness in the range cl of 35 nm to 50 nm and the h of 0 nm to 9 nm did not affect the plasmonic dip movement much. On the other hand, the roughness outside this regime dramatically

degraded the sensitivity, and the roughness height h affected the dip movement more than the roughness period. In the next section, the FWHM will be analyzed to quantify the effect of the roughness on the FWHM. A sensitive sensor requires high sensitivity and a narrow FWHM, based on Equation (7).

3.3. Effect of Roughness on the SPR Full Width at Half Maximum (FWHM)

Figure 10a showed the average FWHM of the SPR reflectance dip when the refractive index was 1.33 and 1.35, as calculated using Equation (4) and the methods described in Sections 2.1–2.3 for different roughness profiles. The narrowest SPR dip occurred at h of 1 nm and cl of 50 nm, as shown in Figure 10b. The h parameter had a more substantial effect on the FWHM than the cl parameter, as shown in Figure 10a. Figure 10c shows widened SPR dips due to the surface roughness h of 7 nm and cl of 15 nm.

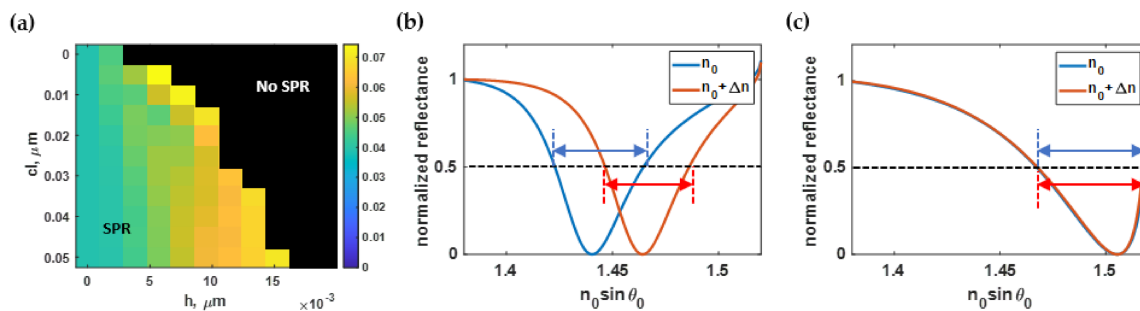


Figure 10. (a) The full width at half maximum in rad/μm calculated using Monte Carlo simulation, (b) SPR dips at h of 1 nm and cl of 50 nm with an average FWHM of 0.04 rad/μm; and (c) SPR dips at h of 7 nm and cl of 15 nm with an average FWHM of 0.05 rad/μm.

The region of interest of the FWHM contour illustrated in Figure 10a was normalized to its maximum value and curve-fitted to the polynomial function $FWHM(h, cl)$ using the built-in curve-fitting toolbox in MATLAB. Figure 11a shows the curve-fitted contour calculated based on Equation (9). The R^2 of the curve-fitted model was 99.95%. In addition, the absolute values of the residue between the equation-based model and the RCWA simulations are shown in Figure 11b.

$$\begin{aligned}
 FWHM(h, cl) = & 0.71 + 403.5h - 14.1cl - (1.75 \times 10^4)h^2 - (2.51 \times 10^4)hcl \\
 & + 364.5cl^2 - (4.09 \times 10^6)h^3 + (2.10 \times 10^6)h^2cl \\
 & + (4.90 \times 10^5)hcl^2 - 3101cl^3 + (5.93 \times 10^8)h^4 \\
 & - (7.61 \times 10^7)h^3cl - (2.90 \times 10^7)h^2cl^2 - (2.94 \times 10^6)hcl^3 \\
 & - (1.78 \times 10^{10})h^5 - (4.36 \times 10^9)h^4cl + (1.98 \times 10^9)h^3cl^2 \\
 & - (2.23 \times 10^7)h^2cl^3
 \end{aligned} \quad (9)$$

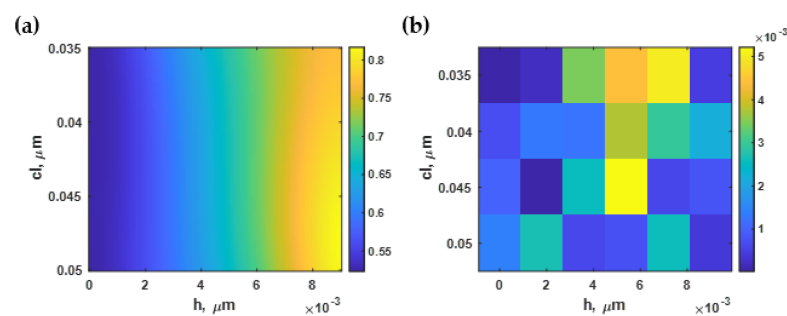


Figure 11. (a) The normalized full width at half maximum using Equation (9); and (b) the difference between Equation (9) and the RCWA simulation.

The curve-fitted contour in Figure 11a indicated that the FWHM was not affected by the roughness period cl ; on the other hand, the FWHM was mainly affected by the roughness height h . The h below 1 nm did not degrade the sensitivity or the FWHM. The RMS roughness extracted from reported fabrication processes was around 1 nm, as shown in Table 1. If the dentition of FOM were only the sensitivity over the FWHM, as usually employed in several articles [69,70], the FOM of the smooth gold sensor and the gold sensor with the roughness of cl of 50 nm and h of 1 nm were 30.49 RIU⁻¹ and 29.98 RIU⁻¹, respectively. In other words, an ideally smooth surface would perform similar to a gold sensor fabricated using the reviewed coating and surface treatment processes, with only a 1.7% difference in sensing performance. Hence, one may conclude that a surface treatment after the coating process is not necessary. Of course, the sensitivity over the FWHM cannot provide a complete story without considering the optical intensity and the signal-to-noise ratio. Since the SPR measures reflectance through attenuated total internal reflection, reflectance spectra usually have a strong background. If the plasmonic dip intensity is not deep, the optical detection measures a weak signal over a strong background, leading to a weak signal-to-noise ratio. Therefore, here we introduced the FOM as expressed in (7). The change in plasmonic dip intensity and the optical signal contrast are investigated and quantified in the following two sections. It will be shown later that the proposed FOM formula could provide a realistic refractive index sensing performance assessment.

3.4. Effect of Roughness on the Intensity Contrast (ΔI)

Figure 12a shows the average intensity change ΔI of the simulated reflectance as the refractive index of the sensing area was altered from 1.33 to 1.35 calculated using Equation (5) for the different constructed rough surface profiles. The surface plasmon resonance with the highest intensity contrast occurred at h of 1 nm and cl of 50 nm, as illustrated in Figure 12b. The intensity difference parameter was significantly reduced as the h increased and cl decreased. At a rougher surface h of 7 nm and cl of 15 nm, the plasmonic intensity of n_s of 1.33 was lower than the n_s of the 1.35 case, as depicted in Figure 12c.

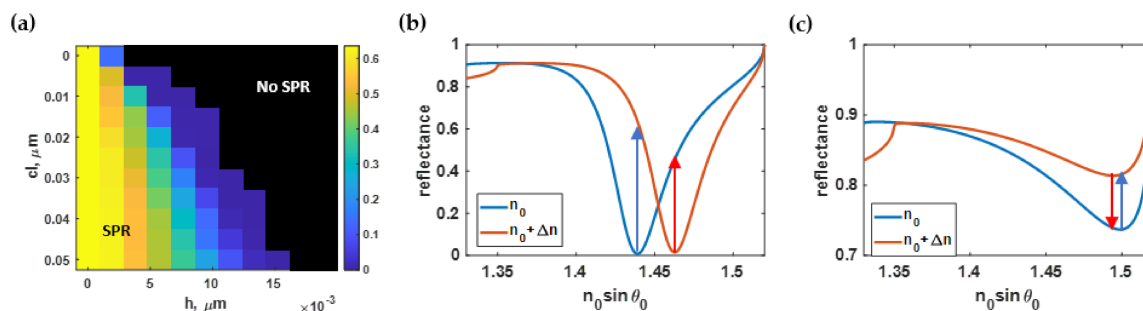


Figure 12. (a) The change in intensity calculated using Monte Carlo simulation; (b) SPR dips at h of 1 nm and cl of 50 nm with an average intensity difference of 0.62; and (c) SPR dips at h of 7 nm and cl of 15 nm with an average intensity difference of 0.004.

The curve-fitting toolbox in MATLAB has then been employed to curve-fit the region of interest of the normalized intensity difference in Figure 12a to the fourth-degree polynomial function $\Delta I(h, cl)$ with an R^2 of 99.86%. Figure 13a,b show the contour plot based on the curve-fitted Equation (10) and the absolute values of the residue between the equation-based model and the RCWA model, respectively.

$$\begin{aligned} \Delta I(h, cl) = & 2.78 - 1882h - 123.3cl + 8375h^2 + (1.27 \times 10^5)hcl + 2804cl^2 \\ & + (3.19 \times 10^6)h^3 - (1.79 \times 10^6)h^2cl - (2.79 \times 10^6)hcl^2 \\ & - (2.09 \times 10^4)cl^3 - 10^8h^4 - (3.61 \times 10^7)h^3cl \\ & + (2.94 \times 10^7)h^2cl^2 + (1.99 \times 10^7)hcl^3 \end{aligned} \quad (10)$$

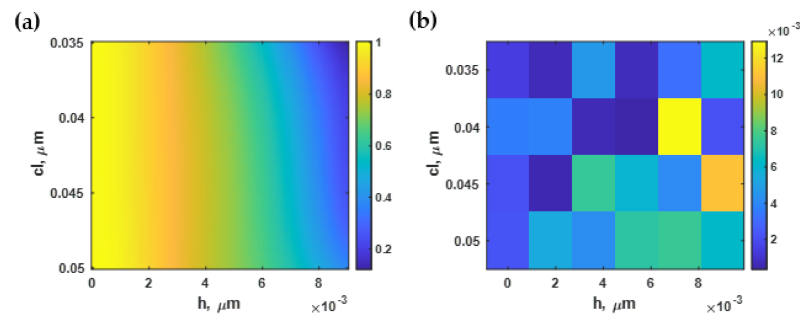


Figure 13. (a) The normalized intensity difference using Equation (10); and (b) the difference between Equation (10) and the RCWA simulation.

Similar to the sensitivity and the FWHM, the optical intensity contrast at the plasmonic dips was mainly affected by the roughness height, not the roughness period. The lower roughness height had a stronger optical contrast, which dramatically declined when the roughness height was more than 8 nm. However, when the h was below 2 nm, the intensity contrast decreased by only 10%, as depicted in Figure 13a. In the next section, the optical intensity at the plasmonic angle is analyzed.

3.5. Effect of Roughness on the SPR Dip Intensity (I_{sp})

The average dip intensities I_{sp} calculated using Equation (6) for different rough surfaces of the computed surface plasmon resonance spectrum with the refractive index of 1.33 and 1.35 are shown in Figure 14a. Similar to the full width at half maximum, the average roughness h had a more substantial effect on the dip intensity than cl , as illustrated in Figure 14a. The smoothest simulated surface (h and cl equal to 1 nm and 50 nm, respectively) gave the lowest dip intensity, as displayed in Figure 14b, and dramatically escalated as the roughness increased (Figure 14c).

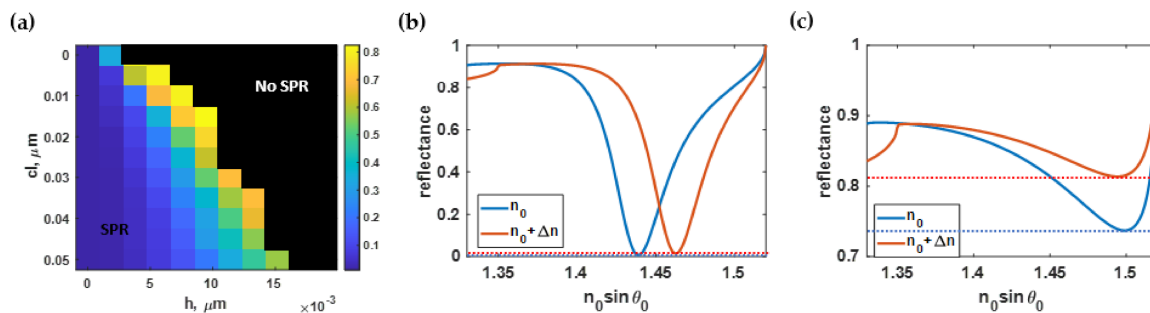


Figure 14. (a) The dip intensity calculated using Monte Carlo simulation; (b) SPR dips at h of 1 nm and cl of 50 nm with an average dip intensity of 0.01; and (c) SPR reflectance spectrum at h of 5 nm and cl of 10 nm with an average dip intensity of 0.78.

The area of interest of the dip intensity contour displayed in Figure 14a was then normalized to the maximum value and then curve-fitted to the fifth-degree polynomial function $I_{sp}(h, cl)$ with an R^2 of 99.82% using the built-in curve-fitting toolbox in MATLAB. The curved-fitted model, expressed in Equation (11), was then employed in the contour plot shown in Figure 15a. Finally, the absolute residue between the RCWA simulated contour and the equation-based contour is illustrated in Figure 15b.

$$\begin{aligned}
 I_{sp}(h, cl) = & -1.77 + 1304h + 125.4cl - (1.21 \times 10^4)h^2 - (8.94 \times 10^4)hcl \\
 & - 2899cl^2 + (2.86 \times 10^5)h^3 + (8.93 \times 10^5)h^2cl \\
 & + (2.01 \times 10^6)hcl^2 + (2.21 \times 10^4)cl^3 - (2.88 \times 10^7)h^4 \\
 & + (1.13 \times 10^7)h^3cl - (1.48 \times 10^7)h^2cl^2 - (1.47 \times 10^7)hcl^3
 \end{aligned} \quad (11)$$

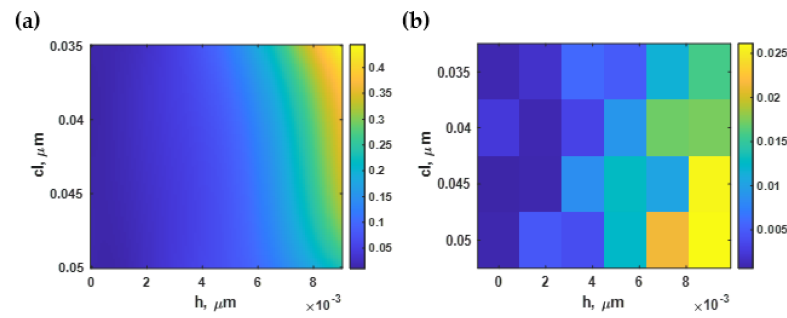


Figure 15. (a) The normalized dip intensity using Equation (11); and (b) the difference between Equation (11) and the simulated output.

The optical intensity at the plasmonic angle was also affected mainly by the h , not the cl like the sensitivity, the FWHM, and the intensity contrast quantified in the earlier sections. The smoother surface provided a deeper intensity dip. However, the change in the optical intensity dip was within only 3%. It will be shown later in the next section that although these performance parameters slightly changed within a roughness range of 2 nm, these performance degradations could accumulate, resulting in the reduced FOM performance in Equation (7) by 50%, reflecting the experimental sensing performance of surface plasmon sensors with different roughnesses reported in Agarwal et al. [51].

3.6. Effect of Roughness on the SPR Figure of Merit (FOM)

The illustration of the FOM of the surface plasmon resonance spectrum calculated using Equation (7) and the procedure described in Sections 2.1–2.3 for different roughness is shown in Figure 16a. The FOM decreased as the h increased and the cl decreased. In other words, the rougher surface led to the worse refractive index sensing capability. This contour was then normalized to the maximum calculated FOM and curve-fitted to polynomial function $FOM(h, cl)$, as expressed in Equation (12), with an R^2 of 99.98%, using the built-in curve-fitting toolbox in MATLAB. Figure 16b shows the curve-fitted contour based on the curve-fitting model. According to Figure 16c, the model had significantly high accuracy, with the maximum absolute residue between Equation (12) and the RCWA simulated contour below 1.6%.

$$\begin{aligned}
 FOM(h, cl) = & -2 - 1181h + 214cl + (1.70 \times 10^5)h^2 + (5 \times 10^4)hcl \\
 & - 5038cl^2 + (2.06 \times 10^7)h^3 - (1.14 \times 10^7)h^2cl \\
 & - (9.68 \times 10^5)hcl^2 + (3.92 \times 10^4)cl^3 - (4.61 \times 10^9)h^4 \\
 & + (4.89 \times 10^8)h^3cl + (1.89 \times 10^8)h^2cl^2 + (6.93 \times 10^6)hcl^3 \\
 & + (2.48 \times 10^{11})h^5 - (2.11 \times 10^{10})h^4cl - (9.18 \times 10^8)h^3cl^2 \\
 & - (1.34 \times 10^9)h^2cl^3
 \end{aligned} \quad (12)$$

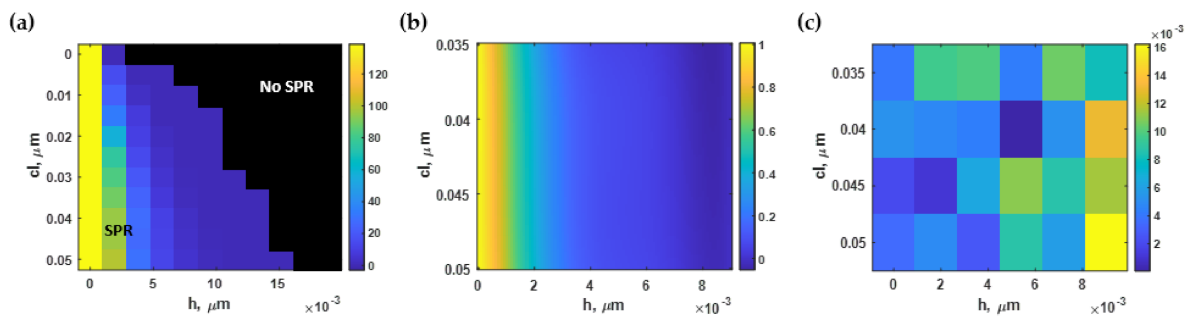


Figure 16. (a) The FOM using Monte Carlo simulation; (b) the normalized FOM based on Equation (12); and (c) the difference between Equation (12) and the RCWA simulation.

The roughness height strongly affected the FOM shown in Figure 16a; meanwhile, the roughness period did not degrade the FOM performance. For example, for a roughness height of 2 nm, the FOM parameter decreased by 50%. Next, we adopted the analysis to quantify the literature's expected refractive index sensing performance of different deposition and surface smoothing techniques.

3.7. Plasmonic Sensing Responses of Different Depositions and Surface-Treatment Technologies

Table 2 shows the performance parameters calculated for the idealized smooth surface and different plasmonic gold sensor roughness reported in the literature for different deposition technologies and surface treatments calculated using Equations (8)–(12). The surface RMS reported in the literature were extracted from each of the referenced articles in Table 2 and then converted to corresponding h and cl values using Equation (2), assuming the h and $1/cl$ had a similar length, as reported by Agarwal et al. [51]. Note that from the above analysis, the cl did not affect the sensitivity, the FWHM, the intensity contrast, or the FOM much compared to the roughness height, as discussed in the earlier result sections. For the sensitivity, all the gold surfaces had a similar performance, indicating the roughness did not affect how far the plasmonic dip moved. For the plasmonic angle, the plasmonic dip for the ideally smooth surface had the lowest plasmonic angle of 71.40° , the same as the other treatment methods with an RMS of less than 1 nm. The sputter coating with no additional treatment method, chemically grown single-crystalline gold, and thermal annealing had a slightly larger plasmonic angle. The FWHM was narrowest for the smooth surface and slightly increased for other coating and treatment techniques. The ΔI performance was similar for all the cases, implying that there was no need for additional surface treatment for the SPR measurement relying on measuring the change in intensity. The intensity dip at the plasmonic angle was strongly affected by the surface roughness, increasing approximately 3.5 times for the nontreated surface compared to the ideally smooth surface. For the FOM calculated using Equation (7), the FOM for the smooth surface was 139.16 and degraded to 90.09 for the sputter-coating technique accounting for 35.26% FOM degradation. Thus, the surface-treatment methods could improve the FOM response for refractive index sensing applications.

Table 2. Refractive index sensing parameters for different surface roughness and smoothing methods.

Method	RMS Roughness (nm)	S (rad · RIU ⁻¹ /μm)	θ_{sp} (Degree)	FWHM (rad/μm)	ΔI	I_{sp}	FOM
Ideal smooth surface	0	7.46	71.40	0.039	0.64	0.007	139.16
No treatment: sputter coating	1.2	7.55	71.51	0.040	0.60	0.024	90.09
Chemical polishing [25,26]	0.38	7.52	71.40	0.039	0.63	0.013	125.20
Mica substrate utilizing [27]	0.2	7.50	71.40	0.039	0.64	0.010	132.16
Chemically grown single-crystalline gold [31]	<1.0	>7.55	<71.51	<0.040	>0.61	<0.021	>98.77
Laser ablation [32]	0.17	7.50	71.40	0.039	0.64	0.010	133.27
Helium ion beam [33]	0.267	7.51	71.40	0.039	0.63	0.011	129.63
Thermal annealing [34]	<1.0	>7.55	<71.51	<0.040	>0.61	<0.021	>98.77

4. Conclusions

There are challenges to overcome for SPR measurements demanding high precision and responsivity, including the environmental fluctuations and the quality of the SPR sensor. In this paper, we proposed a theoretical analysis quantifying the effect of plasmonic gold sensor roughness on its refractive index sensing capability using rigorous coupled-

wave analysis. SPR sensor surface profiles with different roughness heights and roughness periods were modeled using a digital random number generator and a low-pass filter to limit the spatial frequency of the roughness to mimic the surface morphology reported in the literature. The Monte Carlo simulation was then applied to calculate the average plasmonic reflectance spectra for the roughness profiles; the sensing performance parameters, including the sensitivity, the full width at half maximum, the plasmonic angle, the plasmonic intensity at the SPR dip position, the change in optical reflectance and the figure of merit, were computed for different surface roughness profiles. Here, we also proposed and discussed a figure-of-merit definition considering the signal contrast; the proposed FOM could provide a reasonable estimation of refractive index sensing performance. The analysis agreed with the experimental results for different roughness levels reported in the literature. The performance of surface-plasmon-based sensors can be significantly affected by the roughness height. Different coating technologies and surface-smoothing techniques were analyzed and discussed. The RMS roughness reported in the literature for different deposition and surface treatment technologies were employed and analyzed using the proposed theoretical framework.

In the comparison of the conventional sputter-coated SPR-based sensor with a root-mean-square roughness of 1.2 nm to an ideal smooth surface sensor, the sensitivity, plasmonic angle, full width at half maximum, and intensity at the plasmonic dip increased by 1.18%, 0.16%, 3.61%, and 3.51 times, respectively; while the intensity difference at the plasmonic angle and the figure of merit degraded by 6.04% and 35.26%, respectively. Therefore, for applications demanding high precision and responsivity, SPR sensors prepared by conventional deposition methods alone, such as sputter coating, are insufficient to achieve high refractive index sensing performance. Therefore, it is recommended to post-process the SPR sensors using one of the analyzed surface smoothing techniques.

Author Contributions: Conceptualization, S.P. and S.S.; methodology, S.P.; software, S.S. and S.P.; validation, S.P., S.S., and T.T.; formal analysis, S.P.; investigation, S.P., S.S., and T.T.; resources, S.P.; data curation, S.S.; writing—original draft preparation, S.S.; writing—review and editing, S.P. and T.T.; visualization, S.S.; supervision, S.P. and T.T.; project administration, S.P. and T.T.; funding acquisition, S.P. and T.T. All authors have read and agreed to the published version of the manuscript.

Funding: This work was supported by the Research Institute of Rangsit University (RSU) and the School of Engineering of King Mongkut's Institute of Technology Ladkrabang (KMITL).

Institutional Review Board Statement: Not applicable.

Informed Consent Statement: Not applicable.

Data Availability Statement: Not applicable.

Acknowledgments: We would like to acknowledge resources, fruitful discussion, and suggestions from the College of Biomedical Engineering, Rangsit University, Thailand; and the School of Engineering, KMITL, Thailand.

Conflicts of Interest: The authors declare no conflict of interest.

References

1. Brongersma, M.L.; Kik, P.G. *Surface Plasmon Nanophotonics*; Springer: Berlin/Heidelberg, Germany, 2007; Volume 131.
2. Somekh, M.G.; Pechprasarn, S. Surface plasmon, surface wave, and enhanced evanescent wave microscopy. In *Handbook of Photonics for Biomedical Engineering*; Springer Netherlands: Dordrecht, the Netherlands, 2017; pp. 503–543.
3. Mariani, S.; Minunni, M. Surface plasmon resonance applications in clinical analysis. *Anal. Bioanal. Chem.* **2014**, *406*, 2303–2323. [[CrossRef](#)]
4. Chen, J.; Park, B. Label-free screening of foodborne Salmonella using surface plasmon resonance imaging. *Anal. Bioanal. Chem.* **2018**, *410*, 5455–5464. [[CrossRef](#)]
5. Douzi, B. Protein–protein interactions: Surface plasmon resonance. In *Bacterial Protein Secretion Systems*; Springer: Berlin/Heidelberg, Germany, 2017; pp. 257–275.
6. Drescher, D.G.; Selvakumar, D.; Drescher, M.J. Analysis of protein interactions by surface plasmon resonance. *Adv. Protein Chem. Struct. Biol.* **2018**, *110*, 1–30.

7. Sangworasil, M.; Pechprasarn, S.; Larkthanakhachon, S.; Ittipornnusun, K.; Suvarnaphaet, P.; Albutt, N. Investigation on feasibility of using surface plasmons resonance (SPR) sensor for ultrasonic detection: A novel optical detection of ultrasonic waves. In Proceedings of the 2016 9th Biomedical Engineering International Conference (BMEiCON), Luang Prabang, Laos, 7–9 December 2016; IEEE: New York, NY, USA, 2016; pp. 1–3.
8. Shen, M.; Larkthanakhachon, S.; Pechprasarn, S.; Zhang, Y.; Somekh, M.G. Adjustable microscopic measurement of nanogap waveguide and plasmonic structures. *Appl. Opt.* **2018**, *57*, 3453–3462. [[CrossRef](#)]
9. Suvarnaphaet, P.; Pechprasarn, S. Enhancement of long-range surface plasmon excitation, dynamic range and figure of merit using a dielectric resonant cavity. *Sensors* **2018**, *18*, 2757. [[CrossRef](#)]
10. Suvarnaphaet, P.; Pechprasarn, S. Quantitative Cross-Platform Performance Comparison between Different Detection Mechanisms in Surface Plasmon Sensors for Voltage Sensing. *Sensors* **2018**, *18*, 3136. [[CrossRef](#)]
11. Pechprasarn, S.; Chow, T.W.; Somekh, M.G. Application of confocal surface wave microscope to self-calibrated attenuation coefficient measurement by Goos-Hänchen phase shift modulation. *Sci. Rep.* **2018**, *8*, 8547. [[CrossRef](#)] [[PubMed](#)]
12. Chow, T.W.; Pechprasarn, S.; Meng, J.; Somekh, M.G. Single shot embedded surface plasmon microscopy with vortex illumination. *Opt. Express* **2016**, *24*, 10797–10805. [[CrossRef](#)] [[PubMed](#)]
13. Lan, J.; Ge, J.; Yu, J.; Shan, S.; Zhou, H.; Fan, S.; Zhang, Q.; Shi, X.; Wang, Q.; Zhang, L. Structure of the SARS-CoV-2 spike receptor-binding domain bound to the ACE2 receptor. *Nature* **2020**, *581*, 215–220. [[CrossRef](#)] [[PubMed](#)]
14. Otto, A. Excitation of nonradiative surface plasma waves in silver by the method of frustrated total reflection. *Z. Phys. A Hadron. Nucl.* **1968**, *216*, 398–410. [[CrossRef](#)]
15. Kretschmann, E.; Raether, H. Radiative decay of non radiative surface plasmons excited by light. *Z. Nat. A* **1968**, *23*, 2135–2136. [[CrossRef](#)]
16. Barthes, J.; Bouhelier, A.; Dereux, A.; Des Francs, G.C. Coupling of a dipolar emitter into one-dimensional surface plasmon. *Sci. Rep.* **2013**, *3*, 2734. [[CrossRef](#)] [[PubMed](#)]
17. De Leon, N.P.; Shields, B.J.; Chun, L.Y.; Englund, D.E.; Akimov, A.V.; Lukin, M.D.; Park, H. Tailoring light-matter interaction with a nanoscale plasmon resonator. *Phys. Rev. Lett.* **2012**, *108*, 226803. [[CrossRef](#)]
18. Schasfoort, R.B. *Handbook of Surface Plasmon Resonance*; Royal Society of Chemistry: Cambridge, UK, 2017.
19. Homola, J. Present and future of surface plasmon resonance biosensors. *Anal. Bioanal. Chem.* **2003**, *377*, 528–539. [[CrossRef](#)] [[PubMed](#)]
20. Gaylord, T.K.; Moharam, M. Analysis and applications of optical diffraction by gratings. *Proc. IEEE* **1985**, *73*, 894–937. [[CrossRef](#)]
21. Moharam, M.; Gaylord, T. Rigorous coupled-wave analysis of planar-grating diffraction. *JOSA* **1981**, *71*, 811–818. [[CrossRef](#)]
22. Barer, R.; Tkaczyk, S. Refractive index of concentrated protein solutions. *Nature* **1954**, *173*, 821–822. [[CrossRef](#)]
23. Pechprasarn, S.; Larkthanakhachon, S.; Zheng, G.; Shen, H.; Lei, D.Y.; Somekh, M.G. Grating-coupled Otto configuration for hybridized surface phonon polariton excitation for local refractive index sensitivity enhancement. *Opt. Express* **2016**, *24*, 19517–19530. [[CrossRef](#)]
24. Ashley, J.; D’Aurelio, R.; Piekarska, M.; Temblay, J.; Pleasants, M.; Trinh, L.; Rodgers, T.L.; Tothill, I.E. Development of a β -Lactoglobulin sensor based on SPR for milk allergens detection. *Biosensors* **2018**, *8*, 32. [[CrossRef](#)]
25. Miller, M.S.; Ferrato, M.-A.; Niec, A.; Biesinger, M.C.; Carmichael, T.B. Ultrasoother gold surfaces prepared by chemical mechanical polishing for applications in nanoscience. *Langmuir* **2014**, *30*, 14171–14178. [[CrossRef](#)]
26. Leandro, L.; Malureanu, R.; Rozlosnik, N.; Lavrinenko, A. Ultrathin, ultrasoother gold layer on dielectrics without the use of additional metallic adhesion layers. *ACS Appl. Mater. Interfaces* **2015**, *7*, 5797–5802. [[CrossRef](#)] [[PubMed](#)]
27. Diebel, J.; Löwe, H.; Samori, P.; Rabe, J. Fabrication of large-scale ultra-smooth metal surfaces by a replica technique. *Appl. Phys. A* **2001**, *73*, 273–279. [[CrossRef](#)]
28. Nagpal, P.; Lindquist, N.C.; Oh, S.-H.; Norris, D.J. Ultrasoother patterned metals for plasmonics and metamaterials. *Science* **2009**, *325*, 594–597. [[CrossRef](#)]
29. Hegner, M.; Wagner, P.; Semenza, G. Ultralarge atomically flat template-stripped Au surfaces for scanning probe microscopy. *Surf. Sci.* **1993**, *291*, 39–46. [[CrossRef](#)]
30. Gütés, A.; Carraro, C.; Maboudian, R. Ultrasoother gold thin films by self-limiting galvanic displacement on silicon. *ACS Appl. Mater. Interfaces* **2011**, *3*, 1581–1584. [[CrossRef](#)] [[PubMed](#)]
31. Wieduwilt, T.; Kirsch, K.; Dellith, J.; Willsch, R.; Bartelt, H. Optical Fiber Micro-Taper with Circular Symmetric Gold Coating for Sensor Applications Based on Surface Plasmon Resonance. *Plasmonics* **2013**, *8*, 545–554. [[CrossRef](#)]
32. Ng, D.K.; Bholra, B.S.; Bakker, R.M.; Ho, S.T. Ultrasoother gold films via pulsed laser deposition. *Adv. Funct. Mater.* **2011**, *21*, 2587–2592. [[CrossRef](#)]
33. Zhang, C.; Li, J.; Belianinov, A.; Ma, Z.; Renshaw, C.K.; Gelfand, R.M. Nanoaperture fabrication in ultra-smooth single-grain gold films with helium ion beam lithography. *Nanotechnology* **2020**, *31*, 465302. [[CrossRef](#)] [[PubMed](#)]
34. Zhang, J.; Irannejad, M.; Yavuz, M.; Cui, B. Gold nanohole array with sub-1 nm roughness by annealing for sensitivity enhancement of extraordinary optical transmission biosensor. *Nanoscale Res. Lett.* **2015**, *10*, 1–8. [[CrossRef](#)]
35. Pechprasarn, S.; Somekh, M.G. Detection limits of confocal surface plasmon microscopy. *Biomed. Opt. Express* **2014**, *5*, 1744–1756. [[CrossRef](#)]
36. Shankaran, D.R.; Gobi, K.V.; Miura, N. Recent advancements in surface plasmon resonance immunosensors for detection of small molecules of biomedical, food and environmental interest. *Sens. Actuators B Chem.* **2007**, *121*, 158–177. [[CrossRef](#)]

37. Braundmeier Jr, A.; Arakawa, E. Effect of surface roughness on surface plasmon resonance absorption. *J. Phys. Chem. Solids* **1974**, *35*, 517–520. [[CrossRef](#)]
38. Hoffmann, A.; Lenkefi, Z.; Szentirmay, Z. Effect of roughness on surface plasmon scattering in gold films. *J. Phys. Condens. Matter* **1998**, *10*, 5503. [[CrossRef](#)]
39. Rahman, T.S.; Maradudin, A.A. Surface-plasmon dispersion relation in the presence of surface roughness. *Phys. Rev. B* **1980**, *21*, 2137. [[CrossRef](#)]
40. Crowell, J.; Ritchie, R. Surface-plasmon effect in the reflectance of a metal. *JOSA* **1970**, *60*, 794–799. [[CrossRef](#)]
41. Huang, J.-S.; Callegari, V.; Geisler, P.; Brüning, C.; Kern, J.; Prangma, J.C.; Wu, X.; Feichtner, T.; Ziegler, J.; Weinmann, P. Atomically flat single-crystalline gold nanostructures for plasmonic nanocircuitry. *Nat. Commun.* **2010**, *1*, 1–8. [[CrossRef](#)]
42. Chiu, N.-F.; Kuo, C.-T.; Lin, T.-L.; Chang, C.-C.; Chen, C.-Y. Ultra-high sensitivity of the non-immunological affinity of graphene oxide-peptide-based surface plasmon resonance biosensors to detect human chorionic gonadotropin. *Biosens. Bioelectron.* **2017**, *94*, 351–357. [[CrossRef](#)]
43. Kurihara, K.; Suzuki, K. Theoretical understanding of an absorption-based surface plasmon resonance sensor based on Kretschmann's theory. *Anal. Chem.* **2002**, *74*, 696–701. [[CrossRef](#)]
44. Otto, A. Investigation of electrode surfaces by surface plasmon polariton spectroscopy. *Surf. Sci.* **1980**, *101*, 99–108. [[CrossRef](#)]
45. Nishida, M.; Matsumoto, T.; Koga, H.; Kosako, T.; Kadoya, Y. Evaluation of surface roughness of metal films using plasmonic Fano resonance in attenuated total reflection. *Phys. Rev. B* **2020**, *101*, 085414. [[CrossRef](#)]
46. Parmigiani, F.; Scagliotti, M.; Samoggia, G.; Ferraris, G. Influence of the growth conditions on the optical properties of thin gold films. *Thin Solid Film.* **1985**, *125*, 229–234. [[CrossRef](#)]
47. Raether, H. The dispersion relation of surface plasmons on rough surfaces; a comment on roughness data. *Surf. Sci.* **1983**, *125*, 624–634. [[CrossRef](#)]
48. Kolomenski, A.; Kolomenskii, A.; Noel, J.; Peng, S.; Schuessler, H. Propagation length of surface plasmons in a metal film with roughness. *Appl. Opt.* **2009**, *48*, 5683–5691. [[CrossRef](#)]
49. Yang, Z.; Liu, C.; Gao, Y.; Wang, J.; Yang, W. Influence of surface roughness on surface plasmon resonance phenomenon of gold film. *Chin. Opt. Lett.* **2016**, *14*, 042401.
50. Hasan, M.R.; Akter, S.; Rahman, M.S.; Ahmed, K. Design of a surface plasmon resonance refractive index sensor with high sensitivity. *Opt. Eng.* **2017**, *56*, 087101. [[CrossRef](#)]
51. Agarwal, S.; Giri, P.; Prajapati, Y.K.; Chakrabarti, P. Effect of surface roughness on the performance of optical SPR sensor for sucrose detection: Fabrication, characterization, and simulation study. *IEEE Sens. J.* **2016**, *16*, 8865–8873. [[CrossRef](#)]
52. Byun, K.M.; Yoon, S.J.; Kim, D. Effect of surface roughness on the extinction-based localized surface plasmon resonance biosensors. *Appl. Opt.* **2008**, *47*, 5886–5892. [[CrossRef](#)] [[PubMed](#)]
53. Tran, N.H.T.; Phan, B.T.; Yoon, W.J.; Khym, S.; Ju, H. Dielectric metal-based multilayers for surface plasmon resonance with enhanced quality factor of the plasmonic waves. *J. Electron. Mater.* **2017**, *46*, 3654–3659. [[CrossRef](#)]
54. Diao, W.; Tang, M.; Ding, S.; Li, X.; Cheng, W.; Mo, F.; Yan, X.; Ma, H.; Yan, Y. Highly sensitive surface plasmon resonance biosensor for the detection of HIV-related DNA based on dynamic and structural DNA nanodevices. *Biosens. Bioelectron.* **2018**, *100*, 228–234. [[CrossRef](#)]
55. Fabini, E.; Danielson, U.H. Monitoring drug–serum protein interactions for early ADME prediction through Surface Plasmon Resonance technology. *J. Pharm. Biomed. Anal.* **2017**, *144*, 188–194. [[CrossRef](#)]
56. Cao, Y.; Griffith, B.; Bhomkar, P.; Wishart, D.S.; McDermott, M.T. Functionalized gold nanoparticle-enhanced competitive assay for sensitive small-molecule metabolite detection using surface plasmon resonance. *Analyst* **2018**, *143*, 289–296. [[CrossRef](#)] [[PubMed](#)]
57. Miyazaki, C.M.; Shimizu, F.M.; Mejía-Salazar, J.; Oliveira, O.N., Jr.; Ferreira, M. Surface plasmon resonance biosensor for enzymatic detection of small analytes. *Nanotechnology* **2017**, *28*, 145501. [[CrossRef](#)]
58. Taylor, A.B.; Zijlstra, P. Single-molecule plasmon sensing: Current status and future prospects. *ACS Sens.* **2017**, *2*, 1103–1122. [[CrossRef](#)]
59. Kabashin, A.V.; Evans, P.; Pastkovsky, S.; Hendren, W.; Wurtz, G.A.; Atkinson, R.; Pollard, R.; Podolskiy, V.; Zayats, A.V. Plasmonic nanorod metamaterials for biosensing. *Nat. Mater.* **2009**, *8*, 867–871. [[CrossRef](#)]
60. Thadson, K.; Visitsattapongse, S.; Pechprasarn, S. Deep learning-based single-shot phase retrieval algorithm for surface plasmon resonance microscope based refractive index sensing application. *Sci. Rep.* **2021**, *11*, 16289.
61. Berini, P. Long-range surface plasmon polaritons. *Adv. Opt. Photonics* **2009**, *1*, 484–588. [[CrossRef](#)]
62. Sreekanth, K.V.; Alapan, Y.; ElKabbash, M.; Ilker, E.; Hinczewski, M.; Gurkan, U.A.; De Luca, A.; Strangi, G. Extreme sensitivity biosensing platform based on hyperbolic metamaterials. *Nat. Mater.* **2016**, *15*, 621–627. [[CrossRef](#)]
63. Garoli, D.; Calandrini, E.; Giovannini, G.; Hubarevich, A.; Caligiuri, V.; De Angelis, F. Nanoporous gold metamaterials for high sensitivity plasmonic sensing. *Nanoscale Horiz.* **2019**, *4*, 1153–1157. [[CrossRef](#)]
64. Johnson, P.B.; Christy, R.-W. Optical constants of the noble metals. *Phys. Rev. B* **1972**, *6*, 4370. [[CrossRef](#)]
65. Sexton, B.; Feltis, B.; Davis, T. Characterization of gold surface plasmon resonance sensor substrates. *Sens. Actuators A Phys.* **2008**, *141*, 471–475. [[CrossRef](#)]
66. Liu, S.; Ma, Y.; Chen, X.; Zhang, C. Estimation of the convergence order of rigorous coupled-wave analysis for binary gratings in optical critical dimension metrology. *Opt. Eng.* **2012**, *51*, 081504. [[CrossRef](#)]

67. Zhang, B.; Pechprasarn, S.; Somekh, M.G. Quantitative plasmonic measurements using embedded phase stepping confocal interferometry. *Opt. Express* **2013**, *21*, 11523–11535. [[CrossRef](#)] [[PubMed](#)]
68. Fu, D.; Choi, W.; Sung, Y.; Yaqoob, Z.; Dasari, R.R.; Feld, M. Quantitative dispersion microscopy. *Biomed. Opt. Express* **2010**, *1*, 347–353. [[CrossRef](#)] [[PubMed](#)]
69. Meng, Q.-Q.; Zhao, X.; Lin, C.-Y.; Chen, S.-J.; Ding, Y.-C.; Chen, Z.-Y. Figure of merit enhancement of a surface plasmon resonance sensor using a low-refractive-index porous silica film. *Sensors* **2017**, *17*, 1846. [[CrossRef](#)] [[PubMed](#)]
70. Li, R.; Wu, D.; Liu, Y.; Yu, L.; Yu, Z.; Ye, H. Infrared plasmonic refractive index sensor with ultra-high figure of merit based on the optimized all-metal grating. *Nanoscale Res. Lett.* **2017**, *12*, 1–6. [[CrossRef](#)]